MULTIPACTING AND REMEDIES OF ELECTRON CLOUD IN LONG BUNCH PROTON MACHINE*

L. Wang, M. Blaskiewicz, H. Hseuh, P. He, Y.Y. Lee, D. Raparia, J. Wei, S.Y. Zhang, BNL, Upton, NY, USA

R. Macek, LANL, Los Alamos, NM, USA

Abstract

The mechanism of electron multipacting in long bunched proton machine has been quantitatively described by the electron energy gain and electron motion. Some important parameters related to electron multipacting are investigated in detail. It is proved that multipacting is sensitive to beam intensity, longitudinal beam profile shape and transverse beam size. Agreements are achieved among our analysis, simulation and experiment. The possible remedies to clearing electron cloud are also investigated.

INTRODUCTION

The problem of transverse instability and beam loss due to electron-proton interaction has persisted over many years. It was first observed at INP PSR in 1965[1]. Shortly thereafter, electron cloud and beam-introduced multipacting was found at CERN-ISR [2, 3]; this instability was detected during the coasting beam operation and was cured using clearing electrodes. More recently, transverse instability was reported in a bunched proton beam in a Proton Storage Ring at Los Alamos National Laboratory (LANL-PSR) [4]. It appeared to be caused by an electron cloud. An instability, which seems to be due to the interaction of electrons and protons, also occurred at the AGS booster [5]. Electron-cloud instability has been found since the 1990s in the PF [6, 7], KEKB [8], PEP-II [9], BEPC [10], PS, and SPS [11-12]. Grőbner suggested that beam-induced multipacting causes an electron cloud to accumulate inside the vacuum chamber [13, 14]. The cloud then interacts with the proton- or positron-beam and hence, destabilizes it. Experimental observations of electron-cloud instabilities differ distinctively for "short bunches" where multibunch multipacting is expected to be important (the PS, SPS, and B factories) and "long bunches" where single-bunch, trailing-edge multipacting probably is dominant. The mechanism of beam-induced multipacting seems quite different for the two.

In this article, we discuss electron cloud build-up in a long proton machine. The PSR is the existing proton machine in which strong electron-cloud instability was reported. Two candidate mechanisms were offered to qualitatively explain this observation [4, 15]. In the first, electrons captured by the beam (e.g., from residual gas ionization or electrons that survive the gap) oscillate in the potential well of the proton beam, emerging at the end of the pulse with energies that depend on initial conditions and the beam's intensity. When these electrons strike the wall, secondary electrons are produced with yields exceeding unity. The secondaries may travel to the opposite wall and reflect or make tertiary electrons. Such interactions with the wall degrade the electrons' energies to a few *eVs*; in these cases, it can take many nanoseconds for them to die out. If a large enough fraction survives the gap, they will accumulate or buildup until the production and loss rates are in equilibrium. The second candidate mechanism is based on what is aptly described as "trailing edge multipactor". Electrons born at the wall near or after the peak of the pulse passes will be accelerated towards the center of the beam and decelerated after passing through it. On the trailing edge of the beam pulse, such electrons will reach the opposite wall with a certain energy gain. If the gain is high enough, then the secondary emission yield (SEY) can exceed unity, resulting in amplification on each successive traversal of the beam pipe.

Many studies have been made of electron-cloud buildup in long-bunch proton machines based on numerical methods [16–20]. We know from PSR experiments and simulations described in this paper that the buildup depends on several factors such as shape of the beam's longitudinal profile, transverse profile, beam intensity, chamber size and SEY among other things. The simulations published to date have not examined many of these parameter variations and in this paper we undertake a more systematic examination of these and compare with experimental results where available. There is a wealth of data from PSR that can be used to compare with these simulations both to benchmark the code and provide a better understanding of the factors that affect the e-cloud buildup.

The analysis of electron motion and energy gain has also been done by former studies [16, 19]. A more detail analysis of electron motion under beam space charge force and dipole magnetic fields have been carried out in this paper. The analysis of electron motion and the electron energy when it hits the chamber surface are significantly helpful on understanding of the mechanism of electron multipacting. We try to explain the simulated electron build-up with our analysis of electron motion. The combination of the analysis of electron motion and the simulation of electron cloud build-up give us a better

understanding of the electron multipacting from the physics point of view. Furthermore, we investigated several important factors related to multipacting one by one, instead of considering them together. Therefore, we can clearly delineate the effect of each one.

This paper is organized as follows.

First, we introduce the SEY and physics model used in the code CLOUDLAND.

Second, we analyze electron motion under the beam's space-charge force and dipole magnetic field. Long bunches can trap electrons which are emitted or exist before the bunch center. On the other hand, electrons emitted after the center of a proton bunch will move straight to the opposite wall's surface. Accordingly, there is no loss of electrons before the bunch's center, which can partly explain why multipacting always occurs at the bunch's tail. The gain in electron energy is analyzed as a function of the beam's longitudinal and transverse profile, its transverse size, and the chamber's size. One very important factor, the longitudinal beam profile factor, is defined. According to this factor, the gain in electron energy is usually bigger at the bunch's tail, which can explain the mechanism of so-called "trailing edge multipactor".

Third, a few significant parameters related to electron multipacting were investigated in greater detail, based on analyses, simulations, and experimental results. Among of them, beam intensity, longitudinal beam profile shape, transverse beam size, beam in gap, peak SEY and energy at peak SEY are demonstrated to be important in multipacting and beam instabilities. Beam instabilities can be sensitive to electrons by ionization since they can be trapped throughout much of the bunch but multipacting is not.

SEY AND THE PHYSICS MODEL

ORNL is constructing a Spallation Neutron Source (SNS), equipped with a high intensity proton storage. As examples, we use the SNS ring and PSR beam in this study. Table 1 shows the beams' parameters. The SNS beam is assumed to be cylindrical with uniform distribution in the transverse plane, and the PSR beam a Gaussian one.

A major unknown factor is the number of electrons born at the wall. In the PSR, this number at any given location is uncertain by at least two orders-of-magnitude.

It is difficult to reliably estimate the electron yield from proton losses. We need to know the grazing angle of incidence very well for the lost protons, and the places where they are lost. We do not have experimental data with the required detail on the parameters of the lost protons. Conceptually, the number of initial electrons born at the wall might be treated as being proportional to the instantaneous line density of protons in the region of interest (assuming the losses are proportional to line density) with the proportionality constant a free parameter to be fixed by comparing the simulations to one set of experimental data. In Table I, a uniform rate of proton loss along the ring (which is far from true in the real machine), and a proton-electron yield of 100 were assumed based on comparing the simulation and experimental data from the PSR. When these proton-generated electrons hit the beam chamber's surface after a period of transit, more electrons, called secondary electrons, are produced. The emission of secondary electrons is an important process for the buildup of the electron cloud. The secondary electrons include three types: backscattered electrons, rediffused electrons, and true secondary electrons [22]. Secondary emission yield is defined as a fraction of the number of electrons emitted from the metal surface to the total number of incident electrons. In cases where the SEY is larger than unity, the number of electrons increases exponentially. This avalanche phenomenon is called multipacting. The yield of backscattered electrons with normal incident angle is

$$\delta_e(E_0) = P_{1,e}(\infty) + [\hat{P}_{1,e} - P_{1,e}(\infty)]e^{-(|E_0 - \hat{E}_e|/W)^p / p}$$

(1)

where E_0 is the energy of the incident electrons. The yield of rediffused electrons with normal incident angle is

$$\delta_r(E_0) = P_{1,r}(\infty)[1 - e^{-(E_0/E_r)^r}].$$

(2)

The yield of the true secondary electrons with normal incident angle is

$$\delta_{ts}(E_0) = \frac{s(E_0/\hat{E}_{ts})\hat{\delta}_{ts}}{s - 1 + (E_0/\hat{E}_{ts})^s}$$

(3)

The variables in Eqs. (1-3), except E_0, are a constant number that depends on the material properties of the chamber's surface.

Table 1 Simulation parameters for the SNS and PSR

Parameter	Description	SNS	PSR
E (GeV)	Beam energy	1.9	1.75
C (m)	Circumference	248	90
N_p	Beam intensity	2.05×10^{14}	5×10^{13}
$a_x, a_y /\sigma_x, \sigma_y$ (mm)	Transverse beam size	28, 28	10, 10
τ_b (ns)	Bunch length	700	250
b (cm)	Beam pipe radius	10	5
P_l	Proton loss rate/per turn	1.1×10^{-6}	4.0×10^{-6}
Y	Proton-electron yield	100	100

Figure 1 shows the SEY used for simulation and Table 2 the secondary emission parameters. The material of the SNS chamber is stainless steel coated with titanium nitride (TiN). The true secondary parameters are based on one of the experimental results in CERN. Cimino recently showed that the yield of reflected electrons with zero energy, $\hat{P}_{1,e}$ in Table 2, could be close to 1 [23]. Therefore, the reflected component plays a major role in δ at low energies. The multipacting strongly depends on the SEY parameters. We focus on the physics of multipacting in this study. In a real storage ring, the measured SEY parameters should be applied in estimating electron multipacting.
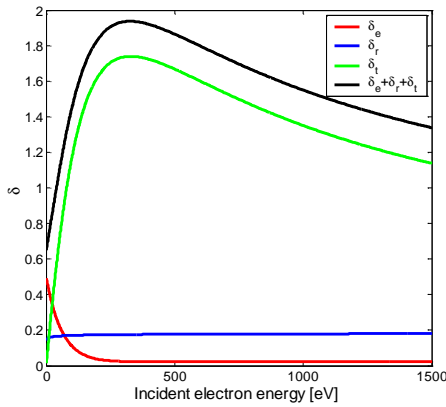

Figure 1 Secondary emission yield

Table 2 Main parameters of SEY used in simulations

Backscattered electrons	
$P_{1,e}(\infty)$	0.02
$\hat{P}_{1,e}$	0.5
$\hat{E}_e(eV)$	0
$W(eV)$	60
P	1
Rediffused electrons	
$P_{1,r}(\infty)$	0.19
$\hat{E}_r(eV)$	0.041
R	0.104
True secondary electrons	
$\hat{E}_{ts}(eV)$	330
$\hat{\delta}_{ts}$	1.74
S	1.526

The simulation program we used is a three-dimensional particle-in-cell (PIC) code named *CLOUDLAND* [21]. It includes the three-dimension electron and proton space charge, beam-electron interaction, and various magnetic fields and electric fields. A primary electron is emitted when a lost proton hits the wall. The electrons move under the beam and its space charge. Inside magnets, the magnetic field also should be included in the calculations. When an electron hits the vacuum chamber's surface, it generates secondary electrons. A statistic distribution

generator obeying the experimental results controls the SEY, energy, and emission angle. Similarly, the secondary electrons may generate tertiary electrons. Because the SEY strongly depends on the energy of the incident electrons, multipacting has very closer relation with electron motion.

PARTICLE MOTION AND ENDGY GAIN

The primary electrons are produced by beam loss at the chamber's surface and ionization at the beam's position. If an electron can oscillate many times under the beam force during the passage of one bunch, then the bunch is called long bunch. Assuming the bunch length is $2\hat{z}$ and the average frequency of electron oscillation is ϖ, a long bunch should satisfy

$$\frac{\hat{z}\overline{\varpi}}{\pi\beta c} >> 1, \qquad (4)$$

where β is the velocity of the proton normalized by the speed of light, *c*. Both the SNS and PSR beam are long beams, wherein the trapped electrons can oscillate more than 50 periods during the bunch's passage.

Magnetic Field Free Region

In the field-free region, the electrons move under the space-charge fields of the proton beam and between other electrons. The space-charge field of the electron cloud can be neglected during the beam's passage because the neutralization factor is small except at the bunch tail where strong multipacting usually happens. Therefore, the electrons' motion during beam passage can be approximated as a movement under the beam's space-charge field only. For the long proton bunch, the longitudinal space-charge field due to potential variations in longitudinal direction also can be neglected because of the slow variation in, and the symmetry of, the longitudinal beam profile that traps the particles in a longitudinal direction. Therefore, the electrons mainly move under the transverse beam fields.

The SNS's transverse beam profile is close to a square with a uniform distribution resulting from correlated painting during injection. Including the space charge causes rapid diffusion in the azimuthal direction and results in round shape [24]. A cylindrical transverse profile is assumed in this paper to approximate the real distribution of the SNS beam.

For a cylindrical beam with a uniform distribution in transverse section, the space-charge fields are

$$E_r(t) = \begin{cases} \dfrac{\lambda(t)}{4\pi\varepsilon_0}\dfrac{2}{r} & (r > a) \\ \dfrac{\lambda(t)}{4\pi\varepsilon_0}\dfrac{2r}{a^2} & (r < a) \end{cases} . \qquad (5)$$

where $\varepsilon_0=10^{-9}/36\pi$ *F/m* is known as the permittivity of vacuum, λ is the beam line density, and *a* is the transverse beams' size. The electron oscillates slowly in longitudinal direction (beam's direction) with small amplitude and

rotates in the azimuth direction with constant angle velocity that depends on the initial condition. Since the motion in the radial direction is uncoupled with the other direction, the nonlinear Hamiltonian of the radial motion is obtained as

$$H = \frac{p^2}{2m} + eU(r,t) \,, \qquad (6)$$

with

$$U(r,t) = \begin{cases} \dfrac{\lambda(t)}{4\pi\varepsilon_0}\left(1+2\ln\dfrac{r}{a}\right) & (r>a) \\[2ex] \dfrac{\lambda(t)}{4\pi\varepsilon_0}\dfrac{r^2}{a^2} & (r<a) \end{cases} \qquad (7)$$

The electron motion in radial direction is a "nearly periodic oscillation" and has a slow time-dependence given by function $\lambda(t)$. Assuming constant λ, the electron will make an exact periodically nonlinear oscillation. In the maximum oscillation amplitude r_{amp}, the kinetic

energy is zero. To get the period of nonlinear oscillations, this is integrated over one-fourth oscillation period

$$T = 4.0 \int_0^{r_{amp}} \frac{dr}{\upsilon(r)} = 4.0 \int_0^{r_{amp}} \frac{dr}{\sqrt{2\Phi e/m}} \qquad (8)$$

with

$$\Phi(r) = \begin{cases} \dfrac{\lambda}{2\pi\varepsilon_0}\ln\dfrac{r_{amp}}{r} & (r>a\,;r_{amp}>a) \\[2ex] \dfrac{\lambda}{4\pi\varepsilon_0}\left(1+2\ln\dfrac{r_{amp}}{a}-\dfrac{r^2}{a^2}\right) & (r\le a\,;r_{amp}>a) \\[2ex] \dfrac{\lambda}{4\pi\varepsilon_0 a^2}\left(r_{amp}^2-r^2\right) & (r\le r_{amp}\le a) \end{cases} \qquad (9)$$

where m is the mass of the electron. Substituting Φ of Eq. (9) for that of Eq.(8), we get the period of nonlinear motion as

$$T = \begin{cases} 4.0\sqrt{\dfrac{\pi\varepsilon_0 m}{\lambda e}}\left(\sqrt{2}a\arcsin\dfrac{1}{\sqrt{1+2\ln(r_{amp}/a)}}+\displaystyle\int_a^{r_{amp}}\dfrac{dr}{\sqrt{\ln(r_{amp}/r)}}\right) & (r_{amp}>a) \\[3ex] 2\pi a\sqrt{\dfrac{2\pi\varepsilon_0 m}{\lambda e}} & (r_{amp}\le a) \end{cases} \qquad (10)$$

The electrons by ionization are produced at the beam with radial coordinates smaller than the beam's size. Therefore, these electrons will oscillate under the linear force. However, the electrons produced by beam loss at the beam pipe will oscillate under the nonlinear force. Consequently, oscillator frequency depends on the radial coordinate when $r_{amp}>a$ due to the effect of the nonlinear force.

If the beam line density $\lambda(t)$ does not change very much within one period of electron oscillation,

$$\frac{1}{\omega_e^2}\frac{d\omega_e}{dt} \ll 1, \qquad (11)$$

there is an adiabatic invariant which is defined with canonical variables p and q as

$$J = \oint p\,dq \,. \qquad (12)$$

For the SNS beam, condition (11) is satisfied except during the first and last 20 ns of the bunch's pulse. The total beam pulse is 700 ns. Therefore, the adiabatic invariant exists during most of the beam passage.

For a given oscillation amplitude r_{amp}, $p(r)$ can be written as

$$p(r,t) = \sqrt{2em(U(r_{amp},t)-U(r,t))} \qquad (13)$$

Substituting Eq. (7) and (13) into Eq.(12), we can get the motion invariant

$$J = \begin{cases} \dfrac{\pi r_{amp}^2}{a}\sqrt{\dfrac{me\lambda}{2\pi\varepsilon_0}} & (r_{amp}<a) \\[3ex] 4a\sqrt{\dfrac{me\lambda}{2\pi\varepsilon_0}}\left(\dfrac{\sqrt{2}}{2}x^{1/2}+\dfrac{1+2x}{2}arctg\dfrac{1}{\sqrt{2x}}+\dfrac{\sqrt{2}}{a}\displaystyle\int_a^{r_{amp}}\sqrt{\ln\dfrac{r_{amp}}{r}}\,dr\right) & (r_{amp}>a) \end{cases} \qquad (14)$$

where $x=ln(r_{amp}/a)$.

For a "smooth" longitudinal beam profile (continuous with its derivative), the variation in electron oscillation amplitude due to the variation of beam density's during the bunch passage can be calculated according to Eq. (14). Figure 2 gives an example of the amplitude calculated by Eq. (14) and of frequency by Eq. (10) during the beam's passage. The estimated amplitude, shown as the dashed solid black line in the figure, agrees well with the numerically simulated oscillation amplitude

of the particle. The oscillation frequency, which depends on the amplitude and beam's density, ranges from 20 to 140 MHz.

For a Gaussian beam, the linear oscillation frequency under beam force is

$$f_{x,y} = \frac{1}{2\pi}\sqrt{\frac{2r_e\lambda c^2}{\sigma_{x,y}(\sigma_x+\sigma_y)}} \qquad (15)$$

The oscillation frequency of electrons varies during the passage of the beam. Consequently, the proton beam oscillates coherently at a frequency range different from

the above incoherent oscillation frequency by a factor that depends on the neutralization caused by coupling between electrons and the proton beam. Therefore, electron-proton instabilities can be distinguished from the conventional impedance-caused instability with a width of resonant frequency that depends on the beam. The peak beam spectrum is roughly proportional to $\sqrt{N_p}$ [25-26], and close to the incoherent frequency given by Eq. (10) because the neutralization factor is small. Therefore, Eq. (10) and Eq. (15) can be used to estimate the instability spectrum.
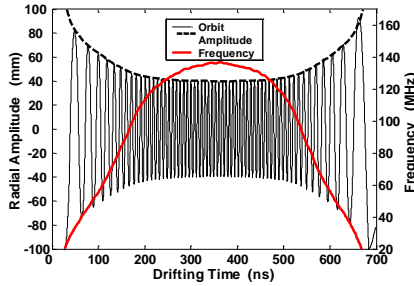
Figure 2 Oscillation amplitude and frequency. The dashed black line is the estimated amplitude.

Figure 3 shows the amplitude contour distribution calculated from the adiabatic invariant for the SNS beam profile, and Figure 4 shows the typical orbit obtained by the CLOULDLAND program; they are consistent. From these two figures, we concluded that

(1) All electrons remaining inside the chamber before the approaching bunch (electrons surviving from the last bunch gap) can be trapped inside the beam during the bunch's passage and be released at its end. The examples of such kinds of electron motion are depicted in Figure 4 with blue and red lines. The blue line shows that electrons surviving from the last bunch gap with oscillation amplitudes about the chamber's radius still can be trapped inside the beam. These surviving electrons from the last bunch gap are important for beam dynamics and cause beam instability because they can be deeply trapped inside beam and their number is huge. They have weak effect on multipacting due to their long term trapping and low energy at the chamber's surface.

(2) The electrons emitted at the pipe's surface between the bunch head and bunch center will oscillate during the beam's passage and hit the chamber wall after the bunch center at the moment

$$t_{hit} \approx t_{emission} + 2(t_{bunchcenter} - t_{emission}) \qquad (16)$$

due to the symmetry of the beam's profile. The earlier the electron is emitted, the later it hits the wall. Electrons emitted at the bunch head could be deeply trapped inside the beam. But more than 95% of primary electrons oscillate with amplitude bigger than the beam's size. The black line depicts such an example of an electron's orbit (Figure 4). It is more clearly shown in Figure 3.

(3) The electrons produced at the beam by ionization can be trapped inside it until the whole bunch passes

them. The pink line in Figure 4 gives the orbit of an electron produced by ionization. These electrons have similar effect as the electrons surviving from the last bunch gap.

(4) The electrons emitted at the chamber's surface after the bunch center will move straight to the opposite chamber wall and produce secondary electrons because there the beam's profile has a negative derivative. (note electrons emitted at the surface move on straight radial lines only if the beam is circular and centered in a cylindrical pipe and if you neglect any non-radial momentum components at the time of emission) The secondary electrons continue cross the chamber until they hit the opposite chamber surface to generate tertiary electrons. As a result, the electrons generated after the bunch center are important for multipacting due to their having a short transit time and sufficient energy when they hit the chamber surface at the bunch tail, as we discuss below. Electrons born at the wall between the bunches' center and tail are the only source of multipacting due to their having a short transit time and sufficient energy when they hit the chamber's surface. We call this kind of electrons multipacting electrons in this paper; all other electrons as described in (1-3) are termed trapped electrons. The green line in Figure 4 plots the orbit of a multipacting electron.

If the transverse beam distribution is round Gaussian, the potential of the beam corresponding to Eq. (7) becomes

$$U(r) = \frac{\lambda}{4\pi\varepsilon_0} \int_0^r \frac{2}{t}\left[1 - \exp\left(-\frac{t^2}{2\sigma^2}\right)\right]dt \qquad (17)$$

Similarly, we obtain the relationship of the electron oscillation amplitudes as in Eq. (12). The PSR beam has an approximately Gaussian distribution in the transverse plane. Figure 5 shows the PSR beam's profile and the oscillation amplitude contour. The contour plots for the SNS and PSR are similar. Electrons can only hit the chamber wall surface after the bunch center. Therefore, multipacting can only occur after the bunch center.
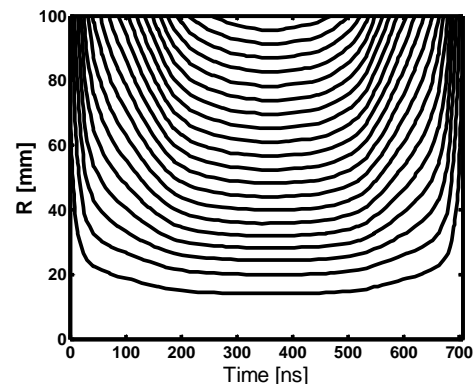

Figure 3 Contour plot of the oscillation amplitude resulting from adiabatic invariant for the SNS beam.
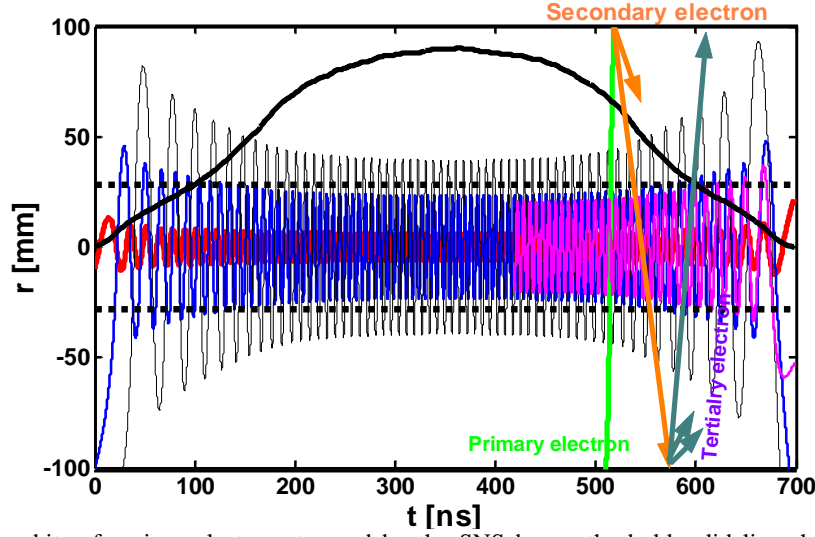
Figure 4 Typical orbits of various electrons trapped by the SNS beam; the bold solid line shows the shape of the longitudinal beam profile and the dashed black lines show its transverse size. The blue and red lines show the orbits of surviving electrons from the last bunch gap. They are trapped inside beam during the beam passage and can cause beam instabilities. The solid back line shows the orbit of the electron which is emitted at the chamber surface between bunch head and bunch center. It oscillates with large amplitude and lost between bunch center and tail. The green line shows the electron which is emitted at the chamber surface between bunch center and tail. It is important for multipacting. It generates secondary and tertiary electrons. The pink line shows the orbit of an electron generated by ionization.
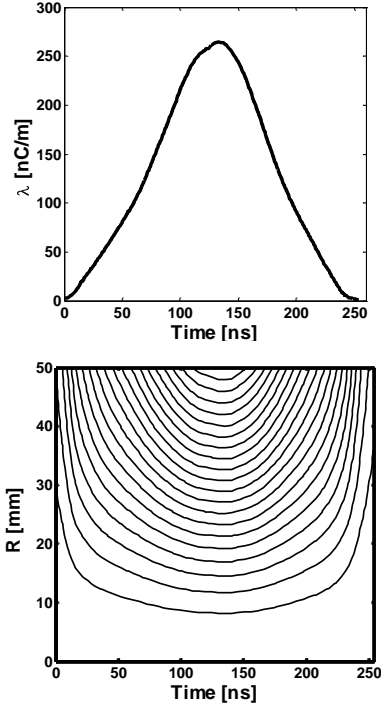

Figure 5 PSR beam profile (top) and electron oscillation amplitude contour (bottom)

The yield of primary-electron emission depends on the rate of beam loss and vacuum pressure. In a real machine, the yield of electrons by beam loss is at least one order-of-magnitude larger than that by ionization. Further, multipacting due to the electrons generated by ionization is very weak for a long bunch as discussed in this paper. As a result, the number of electrons formed by ionization can be ignored compared with those due to beam loss. The electrons by ionization may cause beam instabilities when the vacuum is poor. However, the multipacting due to these electrons is always weak for a long-bunch beam as discussed in the next section. Therefore, we focus only on the electrons due to beam loss in this paper.

For SNS beam, a multipacting electron can hit the chamber surface about 30 times during the period from bunch center to bunch tail. It takes 10 ns to strike the surface once on average. On the other hand, the trapped electron takes long time to hit the surface once (Eq.16). Therefore, only multipacting electrons are important for multipacting due to their short transit time and energy when striking the wall.

Electrons emitted from the chamber's surface between the bunch center and tail are the only source of multipacting. For a multipacting electron, its energy gain from the beam when it hits the chamber surface is [27]:

$$\Delta E = -\frac{1}{2}\beta c\sqrt{\frac{me}{2\pi\varepsilon_0}}\frac{\partial\lambda}{\partial z}\frac{1}{\sqrt{\lambda}}\left(a(2\zeta-1)\arcsin\frac{1}{\sqrt{\zeta}}+a\sqrt{2\ln\frac{b}{a}}+\sqrt{2}\zeta\int_a^b\frac{dr}{\sqrt{\ln(b/r)}}-\frac{1}{\sqrt{2}}\int_a^b\frac{1+2\ln(r/a)}{\sqrt{\ln(b/r)}}dr\right) \quad (18)$$

with $\zeta = 1+2\ln(b/a)$.

Figure 6 compares the energy gain given by Eq. (18) and the numerical method. The blue line is the value obtained by the numerical method and the red line is the energy gain from Eq. (18) that fits the numerical result very well. The initial electron energy when the electron is born is around a few eVs. Therefore, the electron energy when it strikes on the chamber surface is mainly decided by the energy gain from the beam. The electron energy gain at the bunch center is zero due to the zero derivative of beam profile there and it is larger around the bunch tail due to the low beam's line density around there. There are two peaks of energy gain around 550 *ns* where the derivative of the beam profile has two extrema. The maximum energy gain is 300 *eV* around the bunch tail. From the electron energy at the wall surface, we can estimate the SEY. The SEY at different times also is given in Figure 6. It can be concluded from the estimated SEY that multipacting starts at 450ns and it is around 550 ns and bunch tail due to the high energy there. Therefore, the energy gain can clearly explain when the multipacting starts and when it is strong. The mechanism of multipacting can be quantitatively described by Eq. (18).
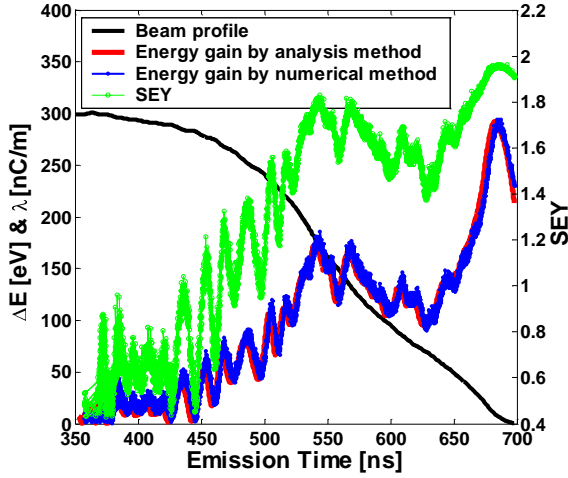

Figure 6 (Color) Comparison of energy gain. The blue line is the energy gain derived by the numerical method, the red line is the energy estimation by Eq. (18), the black line is the beam's profile, and the green line is the estimation of the SEY.

Figure 7 shows the electron density and the current density at the wall during the first 4 turns in one of the drift regions of SNS. The electron cloud begins to build up at 500ns and strong multipacting happens at the bunch tail. This agrees with the data shown in Figure 6. During the bunch's passage, the electron line density inside the beam is almost equal to the line density inside the vacuum chamber, meaning that all electrons remain inside the beam during the bunch passage. Figure 3 and 4 explain this process. Thus, all electrons surviving from the last bunch gap will be trapped inside the beam because their oscillation amplitude is smaller than the beam's transverse size. These electrons interact with beam and can cause beam instabilities. On the other hand, most electrons

linger around the chamber wall's surface at the bunch tail due to the strong multipacting at that moment. It is more clearly depicted in Figure 8 by the transverse distribution of the electron cloud. The electron cloud rapidly decays during the bunch gap due to the space charge effect. The electron line density inside beam is less than 2.0 *nC/m* as shown in Figure 7. The neutralization factor is smaller than 1% except in the bunch head and tail. Therefore, the effect of space charge force among electrons can be neglected comparing with the beam's force.
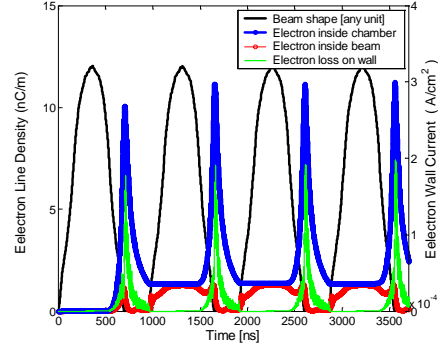

Figure 7 Electron cloud buildup in the SNS drift region. Black line shows the longitudinal beam profile. The blue line is the electron cloud line density inside chamber, which represents the total number of electrons and hence the multipacting. The red line shows the electron line density inside beam. It can drive beam instabilities. The green line gives the current density of electrons striking the wall. It can be used to compare with experiment result.
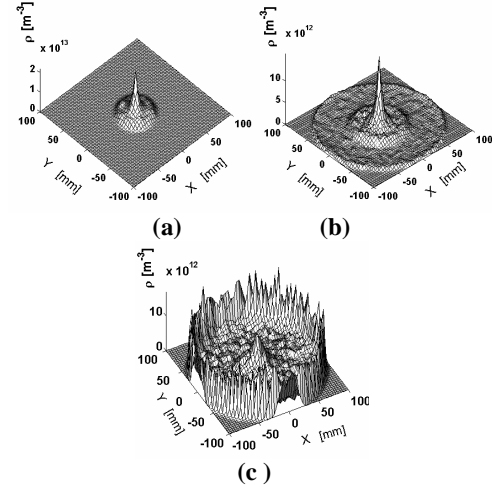

Figure 8 Electron distribution in transverse section at the bunch center (a), 280ns after bunch center (b), and bunch tail (c).

Dipole Magnetic Field

In a strong dipole magnet, an electron can only effectively move along the vertical magnetic field lines. Its vertical motion is similar to the radial motion of an electron in the drift region. For example, the beam's

vertical space-charge field can vertically trap electrons emitted before the bunch's center; electrons emitted from the chamber's surface around the bunch's tail can excite multipacting. Following the same procedure as in the drift region, we can assess the energy gain in a dipole magnet for a multipacting electron moving along the vertical magnetic-field line located at horizontal coordinate X as [27]

$$\Delta E = -c\beta \sqrt{\frac{me}{2\pi\varepsilon_0}} \frac{\partial\lambda}{\partial z} \frac{1}{\sqrt{\lambda}} \left(1 - \frac{X^2}{a^2} + \ln\frac{b^2}{a^2}\right) \left(aG + \int_{\sqrt{a^2-X^2}}^{\sqrt{b^2-X^2}} \left(\ln\frac{b^2}{X^2+y^2}\right)^{-1/2} dy\right)$$

$$+ \frac{1}{2} c\beta \sqrt{\frac{me}{2\pi\varepsilon_0}} \frac{\partial\lambda}{\partial z} \frac{1}{\sqrt{\lambda}} \int_0^{\sqrt{a^2-X^2}} \frac{y^2}{a^2} \left[\ln\left(1 - \frac{X^2}{a^2} + \ln\frac{b^2}{a^2} + \frac{y^2}{a^2}\right)\right]^{-1/2} dy$$

$$+ \frac{c\beta}{2} \sqrt{\frac{me}{2\pi\varepsilon_0}} \frac{\partial\lambda}{\partial z} \frac{1}{\sqrt{\lambda}} \int_{\sqrt{a^2-X^2}}^{\sqrt{b^2-X^2}} \left(1 - \frac{X^2}{a^2} + \ln\frac{X^2+y^2}{a^2}\right) \left[\ln\left(\frac{b^2}{X^2+y^2}\right)\right]^{-1/2} dy \qquad (|X|<a) \qquad (9a)$$

$$\Delta E = -c\beta \sqrt{\frac{me}{2\pi\varepsilon_0}} \frac{\partial\lambda}{\partial z} \frac{1}{\sqrt{\lambda}} \left[\frac{b^2}{X^2} \int_0^{\sqrt{b^2-X^2}} \left(\ln\frac{b^2}{X^2+y^2}\right)^{-1/2} dy - \frac{1}{2} \int_0^{\sqrt{b^2-X^2}} \frac{X^2+y^2}{X^2} \left(\ln\frac{b^2}{X^2+y^2}\right)^{-1/2} dy\right] \qquad |X|>a \qquad (19b)$$

where $G = \arcsin\left[\frac{\sqrt{a^2-X^2}}{a} \left(1 - \frac{X^2}{a^2} + \ln\frac{b^2}{X^2+a^2}\right)^{-1/2}\right]$.

Figure 9 shows the relationship of the electron's energy gain at the wall surface with the X-coordinate. The energy gain has a peak value at the chamber's center that is equal to the energy gain with zero magnetic field, and decreases at both sides. As a result, multipacting in a dipole magnet depends on the horizontal coordinate. It is the strongest at the chamber's center and becomes weak with the increment of $|X|$.
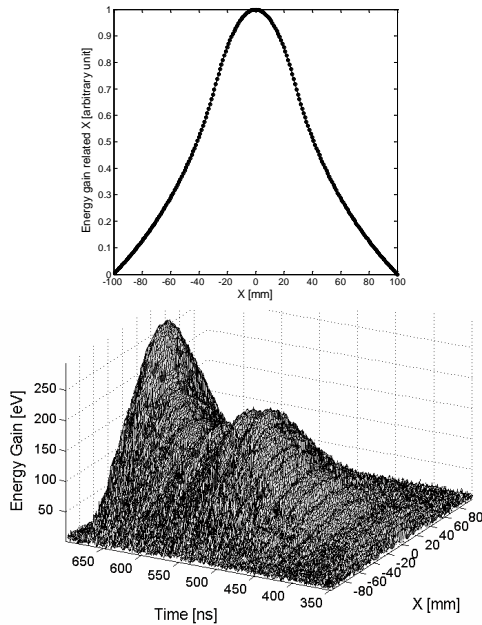

Figure 9 Energy gain at the wall surface for different X-coordinates. The top plot shows the electron energy gain as a function of the horizontal coordinate. It is normalized by the peak energy gain at the chamber's center $X=0$. The bottom plot shows the energy gain of multipacting electrons in the SNS's dipole magnets with $B_y=7935$ Gauss.

IMPORTANT FACTORS IN MULTIPACTING AND BUILD-UP

Multipacting strongly depends on the energy of the electron when it hits the vacuum chamber surface. Accordingly, multipacting is related to the particle's motion. Based on the motion of the electron, a few important factors on multipacting and electron cloud build-up that we studied are discussed in the following paragraphs.

Effects of the Longitudinal Beam Profile and Bunch Length

The effect of the longitudinal beam profile on the electron's energy gain is shown in Eq. (18). The energy gain is governed by the longitudinal beam's profile factor

$$Factor_{profile} = -\frac{\partial\lambda}{\partial z} \frac{1}{\sqrt{\lambda}}. \qquad (20)$$

The first part of the profile factor, the derivative of the line density, represents the difference of beam density between the moments of electron emission and of electron loss. The smaller the beam profile derivative, the smaller is the electron's energy gain. Transit time represents the secondary part in the profile factor. It usually entails a longer transit time round the bunch tail due to the low density of the beam there, and hence, a bigger energy gain. This is the mechanism whereby strong multipacting always happens at the bunch's tail, as shown in Figure 6. The effect of the longitudinal beam profile was first included analytically by Blaskiewicz without further discussion [16]. This effect has been studied in experiments at the PSR [28] and by simulation [17]. The derivative of the longitudinal beam profile was noticed to be important at that time. However, the effect of transit time, which is another one notable factor of multipacting, remains unknown.

Using the same beam profile as in Figure 6, Pivi and Furman [17] artificially truncated the bunch tail while maintaining the same integrated beam charge. The result

of their simulation shows that the electron density can be reduced by a factor more than 100 when the beam profile is cut at 500 *ns.* Comparing this finding with Figure 6, cutting the bunch at 500 *ns* will cut off most of the multipacting area. Figure 6 explains these phenomena.

Figure 10 compares three types of assumed beam profile; Gaussian, sinusoidal, and elliptical. They all have the same integrated beam charge and secondary emission parameters as shown in Table 1 and 2. The figure also has the energy gain and the SEY. Comparing the energy gain and SEY of these three distributions, the Gaussian profile is the worst. Multipacting happens at 375 *ns,* just 25 *ns* after the bunch center and the SEY is almost a constant value close to 2 for long time. The elliptical profile is the best, with multipacting starting later at 600 ns and a smaller SEY. Therefore, the Gaussian profile has the largest peak electron density, 150 *nC/m*, while the elliptical profile has the minimum, of 1n C/m, as shown in Figure 10 (d). A realistic beam profile gives an electron density of about 12 *nC/m*. It is a little worse than the sinuous profile, which gives an electron density 8 *nC/m*. All these findings can be explained by the beam profile factor in Eq. (20). Therefore, the beam longitudinal profile pays a very important role in the multipacting of the long bunched beam.
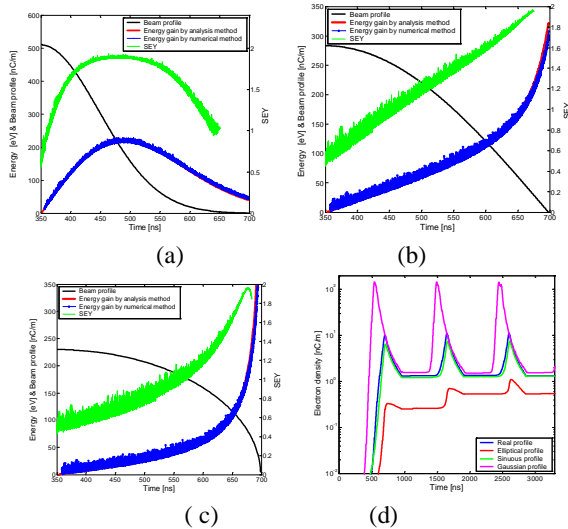

Figure 10 Comparison the effects of a Gaussian, sinuousoidal, elliptical, and realistic beam profile for SNS.

Adjusting the buncher's phase can change the bunch tail. In the PSR, the electron signal at the bunch tail increases 140% when the rf of the buncher phase changes from 281° to 301° due to the increasing tail shoulder [28]. A longer tail causes stronger multipacting at the bunch's tail. However, the instability threshold simultaneously increases by only 26% [29]. The variation in electron clouds inside the beam during the passage of the bunch, proportional to the rate of growth of proton instability [30], is small because of the faster decay in the stronger

multipacting case. Therefore, the measured electron signal at bunch tail is sensitive to the bunch phase, but the instability is less sensitive.

Using the same secondary-electron parameters, Figure11 gives the PSR beam profile, simulated electron energy gain, SEY, and electron cloud build-up in the PSR's drift region. We note that the distribution in the transverse plane of the PSR beam is approximately Gaussian. The electrons inside the beam must fall within $\sqrt{3}$ root mean square (RMS) of the beam's size in order to be consistent with its cylindrical shape. In plotting Figure 11, the longitudinal beam profile factor was multiplied by a constant factor to compare its shape with the energy gain. The energy gain still agrees well with the longitudinal beam profile factor's shape because Gaussian and uniform transverse-beam profiles do not make any difference in the electron's energy gain for the same RMS size, as discussed later. The figure clearly shows that strong multipacting could occur early, just 20 *ns* after the bunch's center. The PSR beam is shorter than the SNS beam, and its total multipacting time is about a factor of two less. However, it has bigger SEY due to the effects of the beam profile. As a result, both beams have almost the same electron cloud density. Note that the same SEY parameters shown in table 2 are used for both the SNS and PSR beam.

Figure 12 shows the measured electron's signal at LANL PSR [31]. The number of electrons grows dramatically at the trailing edge of the proton bunch and it is peak at the bunch tail. This is consistent with the shape of simulated electron wall current (Green line in Figure 11(bottom) and can be clearly explained by the electron energy gain (Blue line in Figure 11(top)). The measured electron energy at the wall is up to 300 *eV*, which roughly agrees with the simulated number 200 *eV*. The discrepancy in electron energy at the wall may come from the difference of the parameters between the simulation and experiment. The wall current due to electron hitting is 0.4 *mA/cm²* determined experimentally [4], and is 0.6 *mA/cm²* by simulation, as shown in Figure 11(bottom).

For a given longitudinal beam profile, the electron density inside chamber slowly changes with the bunch's length provided that the particle density inside the bunch is kept constant by maintaining the bunch's intensity proportional to its length. A long bunch reduces the electron's energy gain but it may increase the possible multipacting time.

If bunch length is reduced, and its intensity kept constant, the electron density inside chamber during the gap will increase quickly with a decrease in bunch length due to both a high gain in energy and fast multipacting frequency for short bunch. However, fewer electrons survive from the last bunch gap when the bunch is shorter due to the stronger space-charge force of the electron cloud at the gap, and the long bunch gap for a short bunch. Simulation shows that a short bunch causes a strong multipacting at its tail and low electron density inside the beam when the bunch length reduces from 700 *ns* to 400 *ns*. Consequently, a short bunch may be a more

stable one. Note that this conclusion depends on the detail parameters. The density of electrons trapped inside beam is the balance effect of multipacting and space charge. The earlier results of a PSR beam study shows that a higher beam current can be stored with shorter bunch length at the same instability threshold [26]. After installing of the inductive inserts [32], the instability threshold curves are unaffected by bunch length variations from 200 to 290 *ns*. This effect is not completely understood, as a shorter bunch length would have smaller momentum spread (for a fixed rf voltage) and provide less Landau damping. However, a short bunch means a longer gap and less chance for electrons to survive the gap. These two effects would tend to cancel.
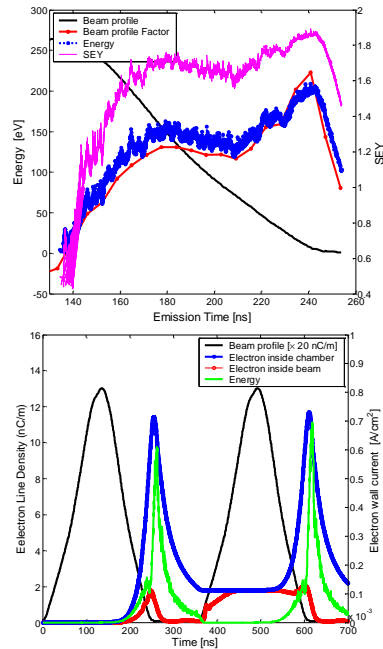

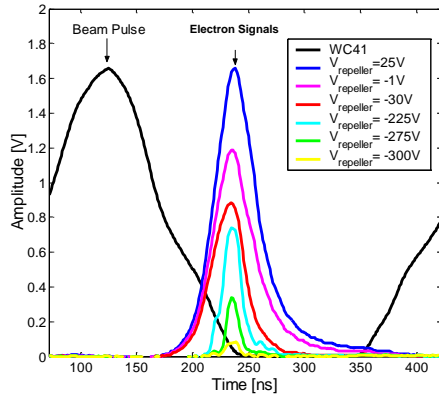Figure 11 Energy gain (top) and electron cloud build-up (bottom) in the PSR drift region

Figure 12 Electron signals measured at the PSR as a function of time relative to the proton-beam pulse during a single revolution for an 8 *μC/pulse* beam. The repeller voltage $V_{repller}$ is varied to select the electrons striking the detector according to their energy.

The Beam's Transverse Profile and Beam Size

Figure 13 plots the build up of the electron cloud and the energy gain for cylindrical beam and Gaussian beam with the same sized RMS in the SNS's drift region. The two transverse profiles exhibit very similar electron densities inside the beam and inside the chamber. The difference in density inside the chamber is less than 5%, while it is equal inside the beam. The underlying explanation is that the space-charge force does not depend on the transverse spatial charge distribution of the beam for a given RMS size [33]. This is confirmed by the electron-energy gain, which is the same for cylindrical beam and Gaussian beam (Figure 13). Therefore, the electron-energy gain of a Gaussian beam can be estimated with the formula used for a cylindrical uniform beam with the same RMS size, as given by Eqs. (18) and (19).

Although the gain in electron energy gain is independent of the beam's transverse profile, the azimuthal distribution of the electron cloud is related to the transverse profile's shape: there is more of the electron cloud in the orientation of the larger beam's size. Figure 14 is a simulated electron-cloud distribution in the transverse plane for an assumed SNS's flat beam σ_x:σ_y=2:1 at different times. The space-charge force in the direction of the larger beam size is stronger and it confines electrons moving along this direction, and then stronger multipacting occurs there. Browman observed a similar phenomenon in the LANL PSR [34]. There is stronger electron signal in the larger betatron function direction.
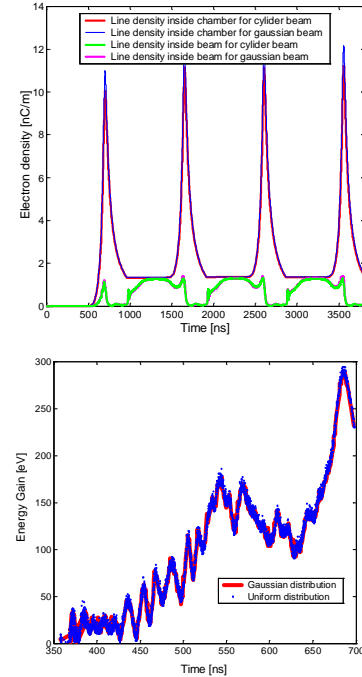

Figure 13 Effect of the transverse beam profile on electron density (top) and electron energy gain (bottom) in the SNS drift region
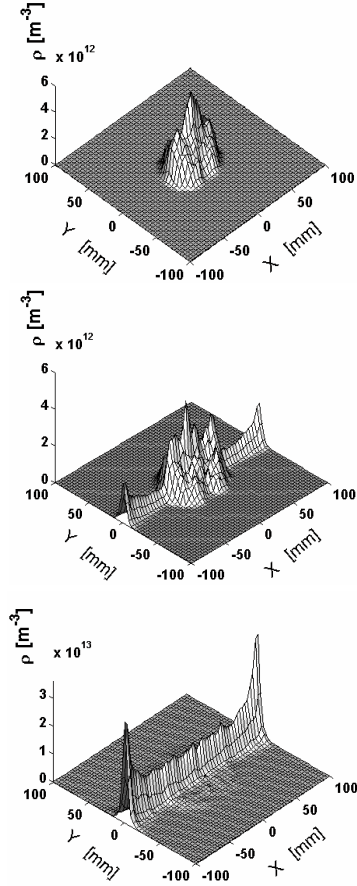
Figure 14 Transverse distribution of electron cloud for an assumed SNS flat transverse beam profile with σx:σy=2:1 at 350 *ns* (top), 560 *ns* (middle), and 630 *ns* (bottom).

The effect of beam size on the energy gain in Eq. (18) is shown in Figure 15(a). A smaller beam size contributes to stronger space-charge field as shown in Eq. (5), and hence, larger electron-energy gain and stronger multipacting. Figure 15(b) demonstrates the effect of the beam's transverse size on the peak electron-cloud line density inside the beam chamber and the average volume density inside the beam. The density inside the chamber is roughly inversely proportion to the transverse beam size. It scales as

$$\lambda_{chamber}[nC/m] = 21 - 0.27a[\text{mm}] \quad (21)$$

However, the electron volume density inside beam is scaled as

$$\rho_{cen}[nC/cm^3] = 4.9e^{-0.1a[mm]}. \quad (22)$$

The volume density inside the beam exponentially decreases with the transverse size of the beam. Therefore, a big beam size is very helpful in reducing beam instabilities caused by the electron cloud. This is consistent with the PSR experimental study [29] wherein the instability threshold rose by a factor two when the beam size was increased from 15 *mm* to 34 *mm*.
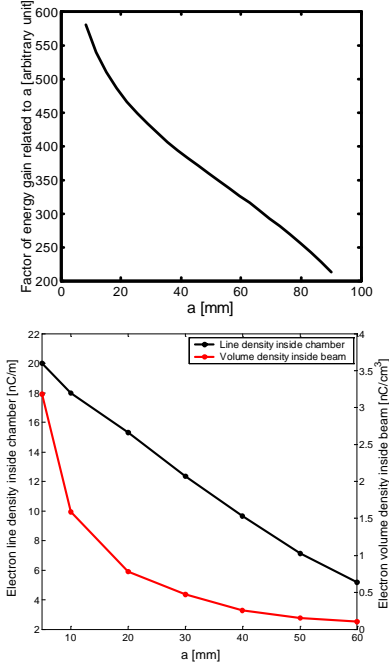

Figure 15 Effect of beam size on electron energy gain (top), and electron cloud density in the SNS drift region (bottom)

Effects of the Beam's Intensity

For a fixed longitudinal beam-profile shape, the energy gain calculated with Eq. (18) is proportional to the square root of the beam's intensity *N*. Figure 16(a) shows the energy gain for the SNS beam, evaluated by the numerical method, for various intensities. The first peaks in the figure are 119 *eV*, 168 *eV*, and 205 *eV* that correspond to $N=1.0\times10^{14}$, $N=2.0\times10^{14}$, and $N=3.0\times10^{14}$. They agree well with Eq. (18).

We kept the total number of lost protons at the same value for different beam intensities to check the latter alone; Figure 16(b) shows the corresponding build-up of electron line density inside the chamber. At high beam density, the density of the electron cloud increases quickly with increments of the beam's intensity, thereby predicating that the former is very sensitive to the latter. This phenomenon can be explained by two mechanisms. One is the plot of energy gain shown in Figure 16(a) showing that a strong beam causes a larger energy gain and hence, a larger SEY. Another more important mechanism is the higher multipacting frequency for a stronger beam. The transit time is inversely proportional to $\sqrt{\lambda}$. Therefore, a more intense beam contributes to a higher multipacting frequency. In the case of $N=2 \times10^{14}$, the maximum number of electrons inside the chamber is 2.2×10^{13} and the total number of primary electrons is 2×10^8. Therefore, on average, one primary electron can produce 1×10^5 secondary electrons at the end of a bunch. Assuming a constant SEY of 2.0, then one primary

electron hits the chamber wall about $\log_2 (1\times10^5)=16$ times with a yield 2.0 during the passage of the whole bunch. If the beam's intensity increases to N', the number of chamber transits per multipacting electron will become $16\sqrt{N'/N_0}$ with $N_0=2.0\times10^{14}$. In this way, we can estimate the electron-cloud density for different beam intensities due to the multipacting-frequency effect. Figure 16(c) shows the relationship of the electron cloud's line density inside the chamber and the beam's intensity obtained by simulation and the estimation method above. They are very close when the beam's intensity is small. However, the discrepancy becomes bigger when the beam intensity increases due to the space-charge effect. We point out that we did not include in the estimation the effect of beam intensity on electron-energy gain and the space-charge effect. By fitting the simulation result, we get the scaling law of electron density with beam intensity as

$$\lambda_{chamber}[nC/m] = 78 - 112\times1.0^{-14}N + 39\times1.0^{-28}N^2 \tag{23}$$

The combined effects of multipacting frequency, energy gain, and the space-charge force causes electron density to grow with the increase in the beam's intensity. In the PSR, the measured electron-cloud signal shows a similar strong dependence on beam intensity [4].

On the other hand, the density of the electron cloud inside the beam becomes saturated, or even may decrease at high beam intensities, as shown in Figure 16(d). When bunch intensity increases, the electron number inside the chamber during the bunch gap also rises, and hence, the space-charge field. The stronger space-charge force entails a short decay time for the electron cloud during the bunch gap. As a result, a high beam intensity affects the electron number inside the beam chamber in two ways: increasing it by stronger multipacting, and reducing it by promoting a quicker decay at the bunch gap due to the stronger space charge. We note that the number of electrons inside the beam roughly equals the number of electrons that survive from the last bunch gap due to the beam field's trapping effect (Figure 4 and 7). This mechanism can explain the saturation or decrease of electron density inside the beam when very strong multipacting takes place.

In LANL PSR, we measured the electron signal when the electrons strike the chamber wall surface, which corresponds to the simulated wall current in Figure 16(d). It is called prompt electron signal. An electron sweeping detector was developed as a diagnostic to measure electrons lingering inside the pipe [35]. Basically it is an RFA with an electrode opposite the RFA. The electrode is pulsed with a short fast pulse (up to 1kV) to sweep low energy electrons at the bunch gap from the pipe into the detector. We call them swept electrons, which corresponds to the simulated surviving the electrons from the bunch gap. Figure 17 shows the measured prompt electron signal and swept electron signal with different bunch intensity in PSR [36]. The prompt electron signal increase without saturation. However, the swept electron signal saturated at

high beam intensity. The increase in the growth of electron cloud density inside the beam and the rise in the electron wall current with an increase in beam intensity, as shown in Figure 16(d), qualitatively agree with the experimental results at the PSR (Figure 16). In PSR's experiments the instability threshold curve are linear up to the maximum intensity we could achieve, i.e., 10 $\mu C/pulse$. According to the physics model, beam instabilities are sensitive to the electrons inside beam and hence the beam instability threshold should saturate at high beam intensity, i.e., 10 $\mu C/pulse$ as shown in Figure 17. The discrepancy between measured electron cloud density and beam instability threshold couldn't be explained.
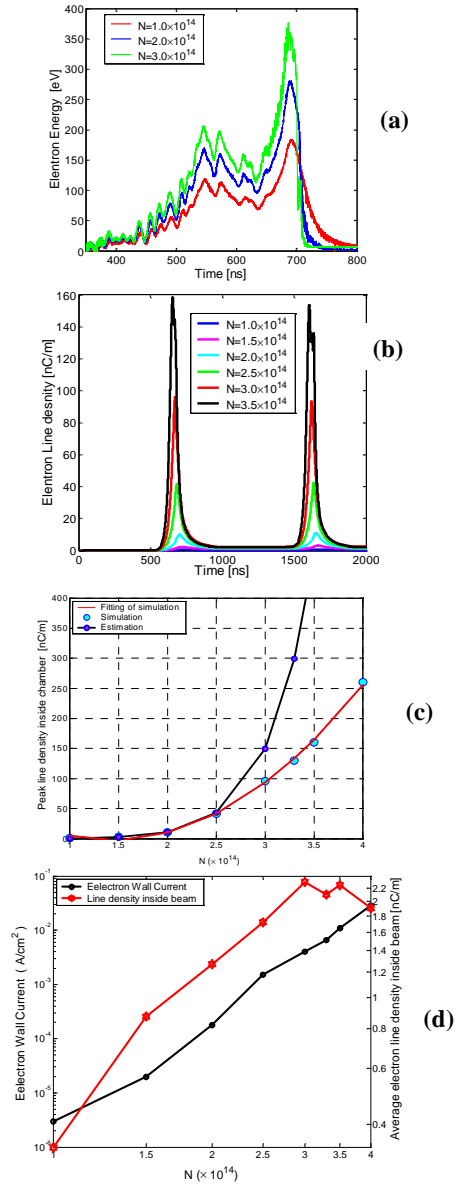
(a)

(b)

(c)

(d)

Figure 16 Beam intensity effects on energy gain (a), electron cloud buildup (b), peak electron density inside the chamber (c), electron wall current, and, average line density inside beam (d) in the SNS drift region
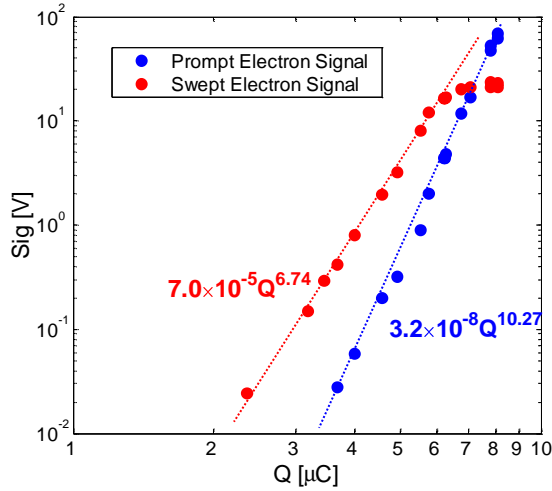
Figure 17 Measured prompt electron and swept electron signal amplitudes are plotted as a function of stored beam intensity in LANL PSR. All other beam parameters were fixed including buncher voltage and accumulation time.

Bunch Gap

The deep trapping effects of the surviving electrons from the last bunch gap play a major role in the operation of the long bunch machine. According to Eq. (14) and Figure 3 and 4, electrons surviving after the bunch gap can be trapped inside the beam until the end of the passage of the next bunch. Electrons inside the beam are the main source of electron-proton instabilities [30]; electrons outside the beam have little effect upon the beam's dynamics. Although strong multipacting occurs at the bunch tail, most electrons remain outside the beam, as shown in Figure 8. The electrons' density inside the beam at the bunch tail is at the same level as at the other times shown in Figures 7 and 11. Therefore, surviving electrons from the last bunch gap cause bunch instabilities.

Note that the bunch gap has a very weak effect on the peak electron line density inside the chamber due to the single-bunch multipacting mechanism. Therefore, the peak electron line density inside the vacuum chamber is almost the same during the passage of the first turn and of the following turns (Figures 7 and 11). However, the bunch gap contributes to reducing the electron density inside the beam. If the gap is long enough, compared with the decay time of the electron cloud during the gap, the electron density inside the beam will be lowered significantly, and hence, the beam's instabilities also. When the bunch gap is short such that the electron cloud cannot decay to zero by the end of the gap, a clearing electrode can be applied to remove the electron cloud. A weak clearing field could be very helpful in reducing the number of electrons inside the beam during the bunch's passage.

The protons remaining at the bunch gap due to their wider momentum spread and a large pulse width can slow down electrons loss at the gap because of its space-charge effect. The percentage of protons at the gap is less than 1×10^{-4} for the SNS design beam. The simulated electron line density inside the chamber increases 18% and 33%, respectively, for 1×10^{-4} and 1×10^{-2} protons at the gap. However, the electron density inside the beam increases 30% and 300%, respectively, due to their slow decay during the gap. Because the growth rate of the beam's instability is proportional to the electron density inside the beam, it follows that instability should be highly sensitive to the beam at the gap, even though that parameter itself has a weak effect on the average electron density inside the chamber.

Effects of Chamber Size

Figure 18 (a) shows that the energy gain in Eq. (18) is almost a linear function of the vacuum chamber's size b. The physics underlying this relationship comes from the transit time. A large chamber imposes a long transit time, and hence, larger gains in energy. Figures 18(b) and (c) show the simulated energy gain and electron cloud buildup for chambers of different sizes. The energy gain is a linear function of b, which agrees with Eq. (18). The SEY is very different for the b=5 cm and 10 cm cases; however, the difference becomes smaller when b increases further because the SEY varies slowly when the incident energy is closer to the energy at peak SEY (Figure 1). It is interesting that the electron density inside the chamber rises with the increment of b and then decreases if b increases further. Two rules govern the character of the electron density with b. A larger b contributes to higher energy and hence, a larger SEY up to the point where the electron energy is at the peak of the SEY curve. However, the electrons' transit time also is longer for a larger b. Consequently, a larger b gives a larger SEY and lower multipacting frequency. Note that while SEY is not sensitive to b when b is large enough, the multipacting frequency is. Therefore, the electron density has maximum value for the median b. For the SNS, this value is 10 cm, which is exactly the radius of the SNS's design chamber. However, the electron density inside the beam increases with the size of b and saturates at around 15cm, as seen in Figure 18.

In a real machine, the beam chamber is big when the size of its local beam is large. In general, the ratio of beam chamber's size to that of the beam is roughly constant along the storage ring. Therefore, both beam chamber and beam size vary along the ring. Figure 19 plots the electron density for different sizes of chambers while keeping the ratio of b to a constant. The electron-cloud line density inside the chamber has peak at the median of b. However, the volume density inside the beam decreases linearly with b. Therefore, employing a large-sized beam and chamber can reduce the beam's instabilities.
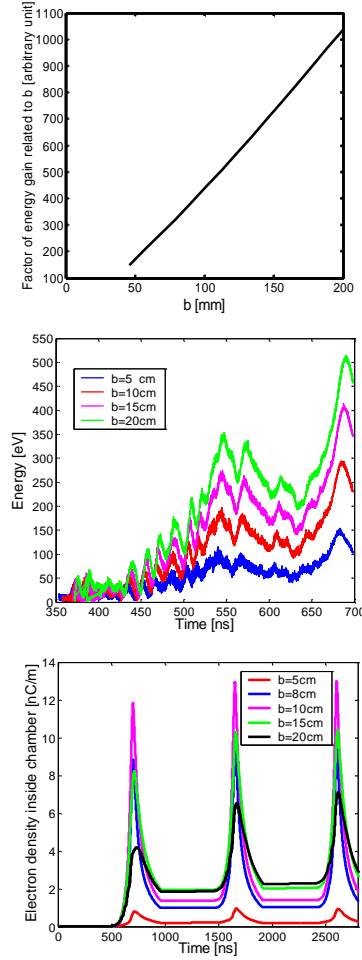
Figure 18 Effect of chamber size on energy gain (top), energy gain for different chamber sizes (middle), and, the buildup of the electron cloud density inside the chamber (bottom) in the SNS drift region with a constant beam size
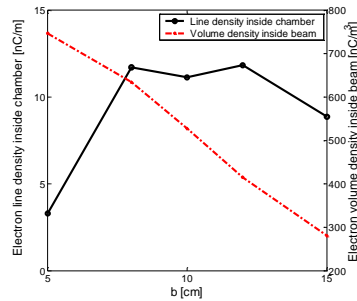

Figure 19 Electron cloud density for different sizes of chambers with a constant *b/a*

Peak SEY and Energy at Peak SEY

It is well known that the density of the electron cloud is very sensitive to peak SEY when multipacting occurs due to its exponential growth. In the absence of a space-charge effect, the electron density should increase exponentially with SEY. Figure 20 shows the electron build-up and electron line density for different peak SEYs. Electron density inside the chamber increases linearly with peak SEY, at a rate that is slower than the exponential growth due to the space-charge effect. In contrast, the average volume electron density inside the beam approaches saturation for a big peak SEY due to the strong space-charge effect. Because beam instability is governed primarily by volume density inside beam, we conclude that the beam's instabilities will saturate at certain peak SEY. However, the heat-load in SNS ring caused by the electron-cloud hitting the chamber does not saturate until the peak SEY is 2.5.

The electron energy gain with a long beam, which usually is less than the energy at peak SEY, is much smaller than that with short bunch, such as in B-Factories. Accordingly, a long beam is more sensitive to the energy at peak SEY. The energy at peak SEY has equivalent effects as the peak SEY. Figure 21 shows the electron build-up and electron density for different energies at peak SEY. Both the electron line density inside the chamber and the electron volume density inside the beam increase linearly with the decrement of energy at peak SEY. The electron volume density inside the beam does not reach saturation because the electron line density inside the chamber is not large enough. For the SNS beam, if the energy at peak SEY in Table 2 falls from 330 *eV* to 246 *eV*, the electron density inside chamber will increase from 12 *nC/m* to 67 *nC/m*. The effect is the same as increasing the SEY from 1.74 to 2.07. However, the effect on electron density inside beam is stronger than increasing the SEY from 1.74 to 2.5. Therefore, a bigger energy at peak SEY can significantly reduce the beam's instability.
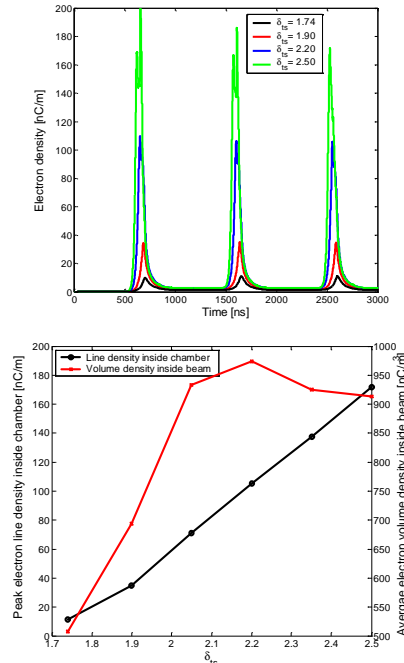

Figure 20 The effects of peak SEY on electron build-up (top) and electron density (bottom).
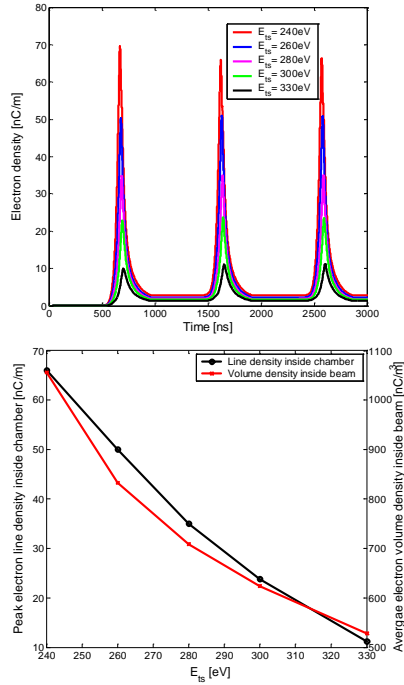
Figure 21   Effects of energy at peak SEY on electron build-up (top) and electron density (bottom).

Electron by Ionization

The number of electrons generated by the residual gas depends on the gas pressure and temperature. The yield usually is more than one order-of-magnitude less than the yield of electrons by proton loss when the vacuum is good depending upon machine design. These electrons have low initial energy [37] and they cannot efficiently obtain energy from the beam when they are released at the end of bunch. Electrons have a maximum energy, 2.7 keV, for the SNS beam when they are created at the bunch's center with radial coordinate a. According to Eqs. (7) and (13), the possible maximum energy gain when an electron is released at the end of bunch is 130 eV. Figure 22 shows the buildup of the electron cloud for the SNS and PSR beams assuming that electrons are initially generated by ionization with a yield same as the yield by proton loss given by Table 1. Note that there is no multipacting for both beams because of the low energy level of the electrons when they hit the chamber wall; the value is below 120 eV for the SNS, and 60 eV for PSR. The electron cloud accumulates slowly due to its long decay time at the bunch gap and the absence of multipacting. The electron-cloud density resulting from ionization is negligible compared with that due to the electrons generated by proton loss for both the SNS and PSR provided their vacuum pressure is satisfactory. When the vacuum is poor, the number of electrons generated by ionization will be notable and all they can be trapped inside beam and cause beam instability without strong multipacting. The electron cloud's density is roughly proportional to the chamber's vacuum pressure due to the lack of multipacting [38]. Unlike electrons, ions liberated

by beam ionization couldn't be trapped by the beam. When the ions hit the chamber surface with sufficient energy, they may create a significant number of electrons born at the wall and then these electrons can excite multipacting with the same mechanism as the electrons by beam loss. The estimation of multipacting by these electrons is under way.
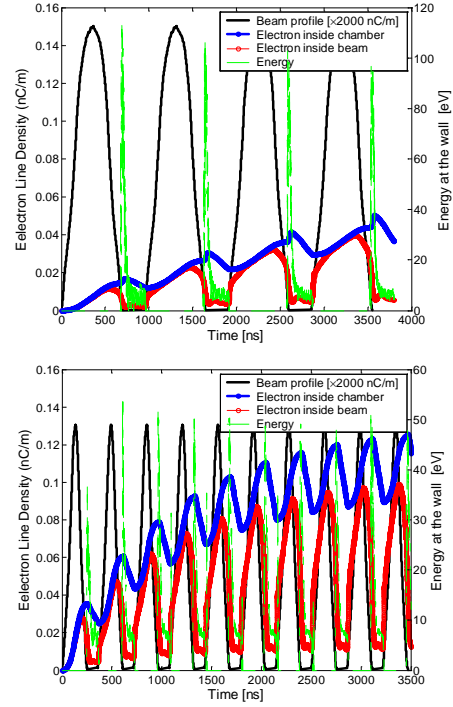

Figure 22   Electron cloud buildup due to ionization in the SNS's (top) and PSR's (bottom) drift region. The beam's profile was reduced by a factor of 2000 so that it could be clearly displayed together with electron-cloud density.

Dipole and Quadrupole Magnetic Fields

In dipole magnets, only electrons moving near the center of the horizontal chamber have enough energy at the wall's surface so that a multipacting cloud forms, as described by Eq. (19) and shown in Figure 9. Figure 23 shows the electron cloud buildup in the SNS's dipole magnet. The electron cloud is about two times smaller than that in drift region due to the limitation of the multipacting area in the dipole magnet. The simulated distribution of the electron cloud in a dipole magnet, shown in Figure 24, is consistent with the gain in electron energy gain (Figure 9). The electron cloud is trapped vertically by the beam's space-charge force at the chamber's center during the beam's passage. Similar to the drift region, there is a strong multipacting at the bunch tail inside the dipole magnet. In the present proton machine, multipacting only can happen at the horizontal chamber's center because electron energy peaks there below a few hundreds eV. It is less than 300 eV in the SNS dipole magnet. However, in short bunch machines, for example the SPS and B-factories, the energy of an electron hitting the wall's surface at the center of the

horizontal chamber could be more than thousands *eV* under normal operational parameters. This causes multipacting at two strips near the chamber's center [11, 21].

Figure 25 shows results of simulations for the electron cloud's transverse distributions in a normal quadrupole magnet. In quadrupole and sextuple magnets, very weak multipacting occurs around the middle of each magnetic pole because only those electrons moving along these field lines could receive enough energy by a mechanism similar to that inside a dipole magnet. The simulated electron cloud is more than two orders-of-magnitude smaller than in the drift region due to the low electron energy at the wall's surface. Quadrupole and sextuple magnet fields are mirror fields that may trap electrons via the mirror-field trap mechanism. However, trapping requires that the bunch length is shorter than the period of gyration [39]. Therefore, electrons emitted from the chamber's surface cannot be trapped in these magnets due to the long bunch length. The electron cloud distribution shown in Figure 25 implies that there is no mirror-field trap; the electron cloud stays closer to the mirror points of the field lines if mirror-field trapping happens. Compared with the electron cloud in the drifting region, the simulated decay time of the electron cloud at the bunch gap in quadrupole and sextupole magnets is much longer due to the weak space-charge effect and the confinement of the electron's orbit by the magnetic fields.
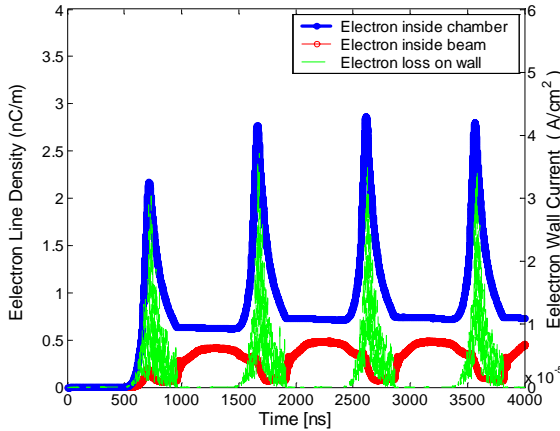

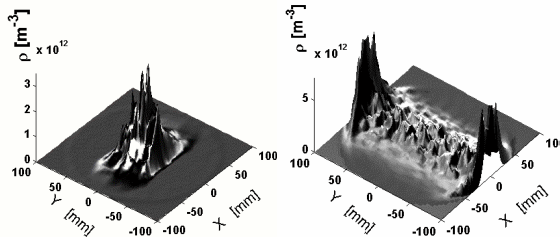Figure 23   Electron cloud build-up in the SNS dipole

Figure 24   Electron cloud transverse distribution in the SNS dipole magnet at bunch center (left) and bunch tail (right)
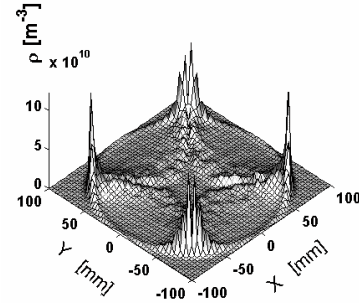

Figure 25 Electron transverse distributions in the SNS's quadrupole.

REMEDIES

A 30 *Gauss* weak solenoid can be invaluable in confining the electron cloud to the region near the wall and limiting the energy of electrons hitting the wall's surface to below the multipacting level. It can reduce the electron density inside chamber by a factor of a thousand. There is a non-electron circle region at the chamber's center with a radius more than the transverse beam's size. Macek's PSR experiment demonstrated that a 20 *Gauss* solenoid field reduces the electron signal by a factor of 50 [28]. We note that the solenoid field in that experiment was nonuniform, which has a weaker effect than a uniform one [40]. Figure 26 shows the electron cloud distribution in a 30G solenoid field.
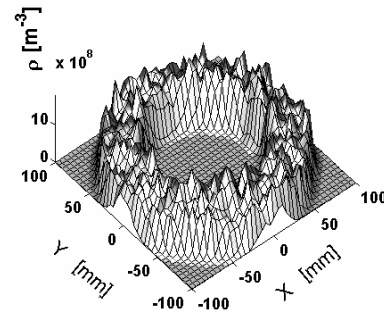

Figure 26 Electron transverse distributions in the SNS's 30G solenoid.

A clearing system was applied to the SNS injection area and the BPMs were modified as clearing electrodes. We assumed a clearing electrode with a vertically uniform field in this study. The clearing field is equal to the total voltage between clearing electrodes divided by the chamber's diameter. In principle, to suppress the electron cloud, a clearing field is required equal to the maximum beam space-charge field at the wall's surface to restrain the emission of secondary electrons. An adequate clearing field should be applied to suppress the emission of secondary electrons at the bunch tail where multipacting occurs. We can estimate the electrons' energy gain using Eq. (18) to find the starting time of multipacting where the total SEY exceeds unity, and then calculate the beam's space charge field near the chamber

wall's surface at that moment. This space charge field is the required electric clearing field to suppress multipacting. For example, at the SNS, a clearing voltage of 8 *kV* is needed to complete suppress multipacting after 500 *ns*. In fact, the requirement on the clearing field is not directly related to the beam's potential because the electrons produced by multipacting at the bunch tail are emitted at the wall's surface and they could not be trapped by the beam's potential, even without any clearing field. The purpose of clearing field is to suppress the emission of secondary electrons instead of pulling them out from the beam's potential like trapped ions or electrons. On the other hand, a necessary condition for removing trapped electrons from a coasting proton beam or ions created by residual gas ionization in an electron machine is that the clearing electrode's electric field should be higher than the maximum field generated by the beam's space-charge because the beams can deeply trap electrons and ions at the chamber's center.

To find the correct clearing field, various clearing voltages were applied, and their effects were simulated using CLOUDLAND. Figure 27 shows the electron peak density at various clearing voltages. As a figure of merit, we use the peak line electron density to describe the clearing field's efficiency. As Figure 27 shows, a notable feature is that this efficiency is not a monotonic function of the clearing voltage. A weak clearing field of 200 *Volts* reduces the line density of the electron by about a factor of 3. Subsequently, the line density increases with the increasing voltage, reaching a maximum at 2,000 *Volts*; it decreases again when stronger clearing fields are applied.
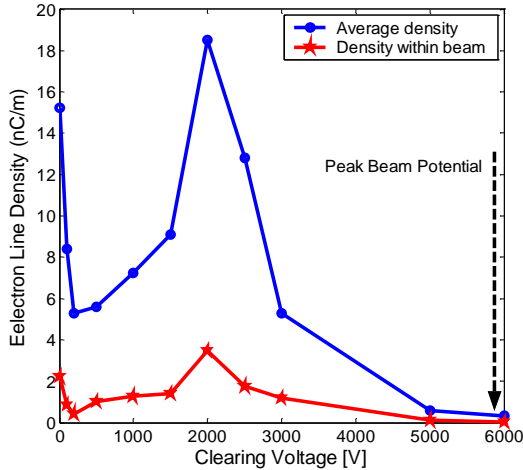

Figure 27. Variation of the peak line density of the electron cloud with various clearing potentials in the SNS's drift region.

It is not surprising that a 6 kV clearing voltage, which equals the beam's peak potential for the SNS ring, can suppress most of the multipacting. We expect 8 kV to complete to suppress it, as discussed above. In agreement with our estimation, we note that the peak potential of 6 kV is not necessary for clearing the electron cloud.

Unexpectedly, however, we found that the clearing efficiency is higher for 200 *Volts* than for 3,000 *Volts*, and that multipacting is stronger with a 2,000 *Volt* clearing field than any other one.

The electron motion in a clearing field can explain these results. Electron motion can be divided into two categories: electrons bouncing between the chamber walls' surfaces with a low clearing field, and bouncing near the positive clearing electrode with a high clearing field.

Without any clearing field, an electron at the bunch tail bounces from one side of the walls' surface to the opposite side and produces secondary electrons that then will rebound. In this case, the electron's energy at the walls' surface ranges from 0 to 300 *eV*. When a low clearing voltage is applied, for example 200 Volts, the electron still bounces between the walls' surfaces. However, the clearing field can effectively reduce the electrons' energy at the surface closer to the negative electrode and increase it at the surface closer to the positive electrode. As a result, the yield of secondary emissions at the latter surface increases while decreasing near the negative electrode due to the relationship between energy of incident electron and the SEY. Therefore, the electron density can be reduced effectively, although multipacting still happens at the surface near the positive electrode. This "alternate multipacting" mechanism ensures that a low clearing field can efficiently lower electron density. The clearing voltage working with "alternate multipacting" mechanism should be smaller than the peak of electron energy gain in zero field case divided by the electron charge *e*, which is 300 *Volts* for SNS's ring.

When the clearing field increases, for example to 500 *Volts*, the electron cannot reach the walls' surface near the negative electrode. Instead, the clearing field turns it back inside the chamber and so the electron reaches the surface closer to the positive electrode than to the location of its genesis until finally, reaches the electrode itself and moves along the vertical lines of the clearing field. This process is quite similar to "clearing field polarization". Without a clearing field, electrons mainly move radially and have uniform azimuthal distribution. The clearing field can change the electron's orbit. The destination of every electron's orbit is the clearing field line. We say that the electrons are finally polarized by the clearing electric field when they move along the clearing field lines. The "polarization time" depends on the strength of the clearing field; the stronger the field, the shorter is the "polarization time".

When an electron bounces only from one side of the chamber's surface, the frequency at which it hits the walls' surface will be reduced by about half, and hence, the density of the electron cloud could be less than when there is no clearing field. The effect of "half multipacting frequency" can explain the result with the 500 *Volts* field. We note that the electron density with the 200 *Volts* clearing voltage is smaller than that with 500 *Volts* (Figure 27) because the alternate multipacting (the

former) results in a lower density compared with the effect of "half multipacting frequency" (the latter). For example, we assume a SEY of 1.8 and 0.7 for the multipacting and no-multipacting case, respectively. The alternate multipacting gives an effective SEY of 1.26 for once multipacting and no-multipacting. In the case of "half multipacting frequency", the chance of multipacting is reduced to half, but the SEY is the same as the multipacting SEY 1.8. Consequently, the "half multipacting frequency" gives an effective SEY of 1.8 that is larger than the effective SEY in alternate multipacting, 1.26.

By further increasing the clearing field, for example, to 2,000 Volts, the multipacting starts earlier around the beam's pulse peak due to the gain in the electron's energy from the clearing field; by contrast, in a low or zero clearing field, multipacting could only happen at the tail of the beam pulse. As a result, there may be stronger multipacting in the presence of a suitable clearing field than in its absence.

The clearing field's effect on the electron's energy when it hits the wall's surface strongly depends on the electron's orbit because the energy received from the clearing field corresponds to the difference in the clearing field's potential between its emission and striking points. If the clearing field is weak, for example 500 $Volts$, the "polarization time" is long, and hence, when the field forces back the electron, the location where it strikes the wall is close to its emission point. Therefore, a weak clearing field has weak effect on the electron's energy at the wall surface during "polarization". However, with a stronger clearing field, "polarization time" is shorter and electron can gather more energy from the clearing field during this process. For examples, the polarization time is 120 ns and 50 ns for 2000 and 5000 $Volts$ cases, respectively. After the electron is polarized, it can no longer receive energy from the clearing field because it will strike on the same position of chamber surface or electrodes. A stronger clearing field generates higher electron energy at the surface but a shorter "polarization time", and hence, short extra multipacting time due to the clearing fields. Therefore, an unsuitable clearing field, 2000 $Volts$, can maximize electron multipacting.

A extreme clearing field, for example 5000 $Volts$, has weak effect on the electrons' energy at the walls' surface except in the very short "polarization time"(about 50 ns), and it can effectively suppress the emission of secondary electrons at the bunch tail where the clearing field could be stronger than the beam's space-charge field at the wall surface. Therefore, a strong clearing field can effectively reduce the electron cloud's density by reducing the chance of multipacting at the bunch's tail, with a weak effect at the bunch's center. A clearing field equal to the maximum beam's space-charge field at the walls' surface will completely suppress multipacting.

Figure 28 shows the transverse distribution of the electron cloud at different times for zero and 2000 $Volt$s clearing voltage. The distribution is azimuthally uniform at zero fields. However, the electron cloud is distributed along the line of the clearing field (vertical here) at the horizontal center due to the "polarization effect" of the clearing field.

The stainless surfaces of vacuum chamber, the injection ceramic chambers and the extraction ferrite kickers are coated with TiN to reduce the SEY [41]. The effect of SEY is clearly shown in Figure 30. The electron density is reduced by one order of magnitude by reducing of SEY from 2.5 to 1.7.

The stripped electrons at the injection region are guided by the magnetic field to the special electron collector located at the bottom the vacuum chamber. The collector can catch most of the stripped electrons with only 0.5% electron can re-enter beam chamber [43].
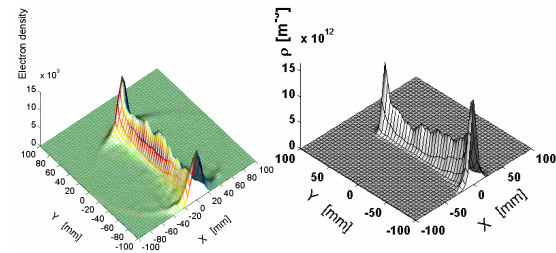

Figure 28. Electron transverse distributions in the SNS with 2kV clearing field at 560 ns (left) at 630 ns (right).

CONCLUSIONS

We have studied in detail electron motion under the beam's space-charge field. The adiabatic invariant clearly describes the oscillation amplitude of the trapped electrons. Combining this data with the longitudinal beam's profile, we readily gained information about the trapped electrons, such as loss time and location. The electrons surviving from the last bunch gap cause proton beam instabilities due to their huge number and deep trapping inside beam during the beam's passage. However, these surviving electrons have weak effect on multipacting because they cannot receive enough energy from the beam. On the other hand, the electrons born at the wall can excite electron multipacting at the bunch tail. Our estimation of the gain in the multipacting electron's energy when it hits the chamber wall is consistent with the numerical result. The energy gain of multipacting electron clearly shows how and when multipacting occurs. According to the longitudinal beam profile factor, the gain in electron energy usually is bigger at the tail of the bunch. In consequence, the multipacting is stronger there. Our analysis quantitatively explains the mechanism of the "trailing edge multipactor".

Various factors related to the electron multipacting were investigated; the beam's longitudinal and transverse profiles, its intensity, the chamber's size, the bunch gap, and the SEY. Among them, multipacting is most sensitive to beam intensity. The electron density grows quickly with increases in the beam's intensity due to the combined effects of multipacting frequency and energy gain.

The longitudinal profile of the beam also plays a very important role on multipacting at the trailing edge. The

longitudinal beam profile factor (Eq.41) can be used to directly estimate the beam profile's effect. According to our study, the bunch tail usually contributes to strong multipacting when the longitudinal beam profile factor is large. That can explain why cutting the bunch tail can effectively reduce multipacting. Thus, we can optimize the design of a real machine to reduce the beam profile factor. The energy spreader and corrector can significantly suppress the beam tail [42] and hence, reduce multipacting.

By contrast, the transverse beam profile has weak effects on electron multipacting. A Gaussian beam and a uniform cylindrical beam of the same RMS size exhibit the same electron-energy gain and electron cloud build-up. A beam with smaller transverse size contributes to stronger multipacting. Electron line density inside the chamber linearly decreases with transverse beam size while the electron volume density inside the beam decreases exponentially. Therefore, beam instability is more sensitive to transverse beam size, and a larger transverse size can weaken the electron-proton instabilities.

The bunch gap is important when the electron cloud's decay time is longer than the gap. In cases where the bunch gap is not long enough to clear the electron cloud, an electric clearing field can effectively do so. The electron cloud surviving from the bunch gap between subsequent bunches, and hence, beam instabilities, also is sensitive to the beam in gap. Multistage beam cleaning that includes multi-step chopping at low energies and beam-in-gap sweeping with collimator collection at the top energy ensures a clean gap.

The secondary emission parameters directly affect electron multipacting. The electron cloud within the chamber shows a roughly linearly increase with the increase of peak SEY in the SNS ring. However, the electron cloud within the beam is saturated at high SEY due to the strong space-charge force at the bunch gap. Except for the peak SEY, energy at the peak SEY also has a very important effect on a long bunch because the maximum gain in energy is close to the energy at the peak SEY. Increasing the energy at peak SEY can significantly reduce multipacting and hence, electron-proton instabilities.

The size of the chamber has both advantages and disadvantages on electron multipacting. Larger chambers entail a larger electron-energy gain and lower multipacting frequency.

With a good vacuum, electrons generated by ionization have a weak effect on the beam's stability due to the absence of multipacting. When the vacuum is poor, these electrons will excite strong electron-proton instabilities because they can be trapped deep inside the beam during its passage.

Multipacting happens at the chamber's center in a dipole magnet. The electron density in dipole magnet is reduced to one-third of the electron density in drift region due to the limitation of multipacting area in dipole magnet. There is a weak multipacting in quadrupole and sextuple magnets where the electron density is two orders-of-magnitude lower than in the drift region. There is no mirror-field trapping in the quadrupole magnet due to the long bunch length. A weak solenoid field up to 30-Gauss can confine all electrons near the wall surface and reduce the electron density with a factor one thousand in the drift region. Clearing electrode works, but its effects is complicated.

ACKNOWLEDGMENTS

REFERENCES

[1] G.I. Budker, G.I. Dimov, V.G. Dudnikov, Proceedings of the International Symposium on Electron and Positron Storage Rings, Saclay, 1966 (Orsay, Universitaiers De France, 1966), page VIII-6-1. .

[2] H.G. Hereward, Coherent instability due to electrons in a coasting proton beam, CERN Report No. 71-15, 1971.

[3] E. Keil and B. Zotter, CERN Report No. CERN-ISR-TH/71-58, 1971

[4] R. J. Macek, A. Browman, D. Fitzgerald, R.C. McCrady, F. E. Merrill, M. A. Plum, T. Spickermann, T. S. Wang, K. C. Harkay, R. Kustom, R. A. Rosenberg, J. E. Griffin, K.Y. Ng, and D. Wildman, Proceedings of the Particle Accelerator Conference, Chicago, 2001 (IEEE, Piscataway, NJ, 2001), p. 688.

[5] M. Blaskiewicz, Workshop on Instabilities of High Intensity Hadron Beams in Rings, edited by T. Roser and S.Y. Zhang, AIP Conf. Proc. No. 496 (AIP, New York, 1999), p. 321.

[6] M.Izawa, Y. Sato, and T. Toyamasu, Phys. Rev. Lett. 74, 5044-5047,1995

[7] K. Ohmi, Phys. Rev. Lett. 75, 1526-1529, 1995

[8] H. Fukuma, Mini-Workshop on Electron Cloud Simulation for Proton and Positron Beams, Proceedings ECLOUD'02, CERN-2002-001, Edited by G. Rumolo and F. Zimmerman, 2002, pp.1-10.

[9] Sam Heifets, Proceedings of 8th Advanced Beam Dynamics Mini-workshop on Two-stream Instabilities in Particle Accelerators and Storage Rings, Santa Fe, New Mexico, USA, 2000. URL: http://www.aps.anl.gov/conferences/icfa/two-stream.html.

[10] Z.Y. Guo, H. Huang, S.P. Li, D.K. Liu, L. Ma, Q. Qin, L.F. Wang, J.Q. Wang, S.H. Wang, C. Zhang, F. Zhou, Y.H. Chin, H. Fukuma, S. Hiramatsu, M. Izawa, T. Kasuga, E. Kikutani, Y. Kobayashi, S. Kurokawa, K. Ohmi, Y. Sato, Y. Suetsugu, M. Tobiyama, K. Yokoya, X.L. Zhang, KEK-PREPRINT-98-23, 1998; also Proceedings of 1st Asian Particle Accelerator Conference, Tsukuba, Japan, 1998, pp 432-434. Edited by Y.H. Chin, M. Kihara, H. Kobayashi, N. Akasaka, K. Nigorikawa, Tobiyama.

[11] J.M. Jiménez, G. Arduini, P. Collier, G. Ferioli, B. Henrist, N. Hilleret, L. Jensen, K. Weiss, F. Zimmermann, "Electron Cloud with LHC-type beams in the SPS : a review of three years of measurements", LHC-Project-Report-632 (2003) .

[12] K. Cornlis, Mini-Workshop on Electron Cloud Simulation for Proton and Positron Beams, Proceedings ECLOUD'02, CERN-2002-001, Edited by G. Rumolo and F. Zimmerman, 2002, pp.11-16.

[13] O. Grőbner, Proceedings of the 10th International Accelerator Conference, Protvino, Russia, 1977 (Institute of High Energy Physics, Protvino, 1977), p. 277.

[14] O. Grőbner, Proceedings of the 17th IEEE Particle Accelerator Conference (PAC 97), Vancouver, Canada (IEEE, Piscataway, NJ, 1998), p. 3589.

[15] R. Macek, "Sources of electrons for stable beams in PSR", PSR Technical Note, PSR-00-10; also V. Danilov, A. Aleksandrov, J. Galambos, D. Jeon, J. Holmes, D. Olsen, "Multipacting on the Trailing Edge of Proton Beam Bunches in PSR and SNS", Workshop on Instabilities of High Intensity Hadron Beams in Rings, edited by T. Roser and S.Y. Zhang, AIP Conf. Proc. No. 496 (AIP, New York, 1999), p. 315.

[16] M. Blaskiewicz, M. A. Furman and M. Pivi, Physics Review Special Topics-Accelerators and Beams, Vol.6, 014203(2003).

[17] M.T.F. Pivi and M.A. Furman, Physics Review Special Topics-Accelerators and Beams, Vol.6, 034201(2003).

[18] K. Ohmi, T. tama and C. Ohmori, Physics Review Special Topics-Accelerators and Beams, Vol.5, 114402(2002).

[19] J. Wei and R. J. Macek, Mini-Workshop on Electron Cloud Simulation for Proton and Positron Beams, Proceedings ECLOUD'02, CERN-2002-001, Edited by G. Rumolo and F. Zimmerman, 2002, pp.29-40.

[20] M.A. Furman and M.T.F. Pivi, LBNL-52872 NOTE 516, 2003, (unpublished)

[21] L. F. Wang, H. Fukuma, K. Ohmi, S. Kurokawa and K. Oide, F. Zimmermann, Physics Review Special Topics-Accelerators and Beams, Vol. 5, 124402 (2002)

[22] M.A. Furman and M.T.F. Pivi, Physics Review Special Topics-Accelerators and Beams, Vol.5, 124404(2002).

[23] R. Cimino, I.R. Collins, M.A. Furman, et. al., CERN-AB-2004-012(ABP), GSI-Acc-Note-2004-02-001, LBNL-54594, SLAC-PUB-10350, 2004

[24] A.V. Fedotov, J. Wei, R.L. Gluckstern, Proceedings of the 2001 Particle Accelerator Conference, Chicago, Illinois, 2001, p. 2851.

[25] R. J. Macek, LANL PSR TECH NOTE, PSR-98-04, 1998

[26] D. Neuffer, E. Colton, D. Fitzgerald, T. Hardek, R. Hutson, R. Macek, M. Plum, Henry A. Thiessen, T.S. Wang, Nucl. Instrum. Meth. A 321, 1992, p.1-12.

[27] L. Wang, M. Blaskiewicz., J. Wei, et. al., Mechanism of Electron multipacting with a long-bunch proton beam, Physical Review E, Vol. 70, (in press)

[28] R. J. Macek, Mini-Workshop on Electron Cloud Simulation for Proton and Positron Beams, Proceedings ECLOUD'02, CERN-2002-001, Edited by G. Rumolo and F. Zimmerman, 2002, pp. 259-268

[29] M. Plum, D. Johnson, R. Macek, F. Merrill, B. Prichard, PSR TECH NOTE, PSR-97-19(1997)

[30] K. Ohmi and F. Zimmermann, Phys. Rev. Lett. 85, p.3821-3823 (2000).

[31] The data collection was done by detector ED42Y in LANL PSR, July 2, 2002, and is documented in Log Book 95, p6-7. Courtesy R. Macek.

[32] K.Y. Ng, D. Wildman, M. Popovic, et. al., Proceedings of the 2001 Particle Accelerator, Conference, Chicago, p2890

[33] B. Houssais, Thesis, Univ. de Rennes, France, 1967.

[34] A. Browman, Proceedings of 8th advanced beam dynamics mini-workshop on two-stream instabilities in particle accelerators and storage rings, Santa Fe, New Mexico, USA, 2000. URL: http://www.aps.anl.gov/conferences/icfa/two-stream.html.

[35] R. Macek, M. Borden, A. Browman, D. Fitzgerald, T.S. Wang, T. Zaugg, K. Harkay, R.A. Rosenberg, Proceedings of the 2003 Particle Accelerator Conference (PAC 03), Portland, Oregon, USA (IEEE, Portland, Oregon, 2003), ROAB003, 2003.

[36] The data was collected in Oct. 7, 2001 for a sweeping detector of PSR, and is documented in Log Book 98, p132-3. Courtesy R. Macek and A. Browman

[37] Lapique F. and Piuz F., Nucl. Instrum. Methods Phys. Res. , 175 (1980) , p.297-318

[38] R. Macek, The 13th ICFA Beam Dynamics Mini-Workshop, Brookhaven National Laboratory, Upton, NY, December, 2003(Unpublished). http://www.c-ad.bnl.gov/icfa/

[39] L. F. Wang, H. Fukuma, S. Kurokawa, K. Oide, Physic Review E, 66, 036502(2002).

[40] L. F. Wang, D. Raparia, J. Wei and S.Y. Zhang, Physics Review Special Topics-Accelerators and Beams, Vol.7, 034401(2004).

[41] H. Hseuh, M. Blaskiewicz, P. He, M. Mapes, R. Todd, L. Wang, J. Wei, S.Y. Zhang, this proceedings.

[42] Jie Wei, Reviews of Modern Physics, Volume 75(2003), p.1383-1432.

[43] L. Wang, Y.Y. Lee, et. al., BNL/SNS Note.